Atmos. Chem. Phys., 9, 9401–9416, 2009
www.atmos-chem-phys.net/9/9401/2009/

Atmospheric Chemistry and Physics

Evidence of ice crystals at cloud top of Arctic boundary-layer mixed-phase clouds derived from airborne remote sensing

A. Ehrlich[1,*], **M. Wendisch**[1,*], **E. Bierwirth**[2,*], **J.-F. Gayet**[3], **G. Mioche**[3], **A. Lampert**[4], **and B. Mayer**[5]

[1]Johannes Gutenberg-University Mainz, Institute for Atmospheric Physics, Mainz, Germany
[2]Laboratory for Atmospheric and Space Physics (LASP), University of Colorado, Boulder, USA
[3]Laboratoire de Météorologie Physique (LAMP), Université Blaise Pascal, Aubière Cedex, France
[4]Alfred Wegener Institute for Polar and Marine Research (AWI), Potsdam, Germany
[5]Institute of Atmospheric Physics, German Aerospace Center (DLR), Oberpfaffenhofen, Germany
[*]now at: Leipzig Institute for Meteorology (LIM), University of Leipzig, Germany

Received: 10 June 2009 – Published in Atmos. Chem. Phys. Discuss.: 23 June 2009
Revised: 4 December 2009 – Accepted: 4 December 2009 – Published: 15 December 2009

Abstract. The vertical distribution of ice crystals in Arctic boundary-layer mixed-phase (ABM) clouds was investigated by airborne remote-sensing and in situ measurements during the Arctic Study of Tropospheric Aerosol, Clouds and Radiation (ASTAR) campaign in March and April 2007. Information on the spectral absorption of solar radiation by ice and liquid water cloud particles is derived from airborne measurements of solar spectral radiation reflected by these clouds. It is shown by calculation of the vertical weighting function of the measurements that the observed absorption of solar radiation is dominated by the upper cloud layers (50% within 200 m from cloud top). This vertical weighting function is shifted even closer to cloud top for wavelengths where absorption by ice dominates. On this basis an indicator of the vertical distribution of ice crystals in ABM clouds is designed.

Applying in situ measured microphysical properties, the cloud-top reflectivity was calculated by radiative transfer simulations and compared to the measurements. It is found that ice crystals near cloud top (mixed-phase cloud top layer) are necessary to reproduce the measurements at wavelengths where absorption by ice dominates. The observation of backscatter glories on the cloud top generally indicating liquid water droplets does not contradict the postulated presence of ice crystals. Radiative transfer simulations reproduce the observed glories even if the cloud top layer is of mixed-phase character.

Correspondence to: A. Ehrlich
(a.ehrlich@uni-leipzig.de)

1 Introduction

Because of low temperatures Arctic boundary-layer mixed-phase (ABM) clouds consisting of both supercooled liquid water droplets and solid ice crystals simultaneously are common. Such clouds have been observed and investigated during numerous Arctic field experiments (Cober et al., 2001; Turner et al., 2003; Korolev et al., 2003; Boudala et al., 2004; McFarquhar and Cober, 2004; Shupe et al., 2008a). As Shupe and Intrieri (2004) have shown, ABM clouds are the most important contributors to the Arctic surface radiation budget. Their radiative impact is highly variable and depends on surface albedo, aerosol particle concentration, cloud water content, cloud particle size and thermodynamic phase (Curry et al., 1996; Shupe and Intrieri, 2004; Ehrlich et al., 2008b). Therefore, an understanding of the physical processes that control the nucleation and spatial distribution of ice crystals and liquid water droplets in such clouds is needed.

A simplified scheme of ABM clouds is presented by Harrington et al. (1999) in which the coexistence of ice and liquid water relies on the balance between the nucleation rate of liquid water droplets and ice crystals, ice crystal growth rate, and removal of ice nuclei by precipitating ice crystals. The persistence of updrafts responsible for the formation of liquid water droplets by condensation is ensured by radiative cooling at cloud top and heat release of the open sea. In this scheme liquid water droplet nucleation is most efficient within updrafts at cloud top and exceeds the ice crystal nucleation rate. This process leads to the typical vertical structure of ABM clouds with a cloud top layer dominated by liquid

Published by Copernicus Publications on behalf of the European Geosciences Union.

water and a layer dominated by ice and precipitating ice crystals below (e.g., Pinto, 1998; Shupe et al., 2006; McFarquhar et al., 2007).

This simplified scheme is modified by a number of factors which need to be maintained in equilibrium to assure the persistence of such clouds. Even slight changes (e.g. an increase of the ice crystal nucleation rate or a decrease of the ice crystal sedimentation rate) may result in a complete glaciation of the cloud as shown by Harrington et al. (1999). A glaciation will shorten the life time and alter the radiative properties of these clouds significantly. In this regard ice crystal properties and ice nuclei play a crucial role by controlling the ice crystal concentration. However, nucleation, growth, and sedimentation of ice crystals are still not well understood which leads to discrepancies between observed and simulated ice crystal number concentrations (e.g., Morrison et al., 2008; Fan et al., 2008). As a consequence, results of cloud-resolving dynamical models are highly sensitive to the parameterizations of these processes as shown by, e.g., Harrington et al. (1999); Morrison et al. (2005); Prenni et al. (2007). Morrison et al. (2005) analyzed the importance of different ice production processes while Harrington et al. (1999) investigated the dependence of the life time of ABM clouds on temperature, ice crystal number concentration, and ice crystal shape and found that the concentration of ice nuclei is the most determining parameter. An increase of the ice nuclei concentration results in a rapid glaciation of the cloud and reduces its life time. The concentration of cloud condensation nuclei which typically ranges magnitudes above ice nuclei concentrations has a minor impact.

These uncertainties in simulations of ABM clouds suggest that information on ice crystal properties is needed. Especially the vertical distribution of ice crystals will help to identify ice nucleation processes that are associated with distinct cloud layers (e.g. evaporation freezing at cloud top and cloud base).

Ground-based remote sensing of Arctic clouds and in situ measurements of ice crystal microphysical properties such as ice crystal size, number concentration and shape have been conducted for many years. For example, parameterizations of the ice volume fraction (ratio of ice to total water content) as a function of cloud temperature have been obtained from in situ measurements by Boudala et al. (2004); Korolev et al. (2003). From ground-based remote-sensing instruments it could be shown that even though the cloud top of ABM clouds is dominated by liquid water, ice crystals exist throughout the clouds with a maximum in lower cloud layers (Shupe et al., 2006, 2008a,b; de Boer et al., 2009). This was confirmed by McFarquhar et al. (2007) who investigated the vertical distribution of ice crystals by in situ measurements. However, due to limitations in time and/or space, in situ measurements and ground-based measurements can only give a snapshot of the complexity of Arctic clouds (Lawson et al., 2001; Cober et al., 2001; McFarquhar et al., 2007; Gayet et al., 2009). To globally and continuously derive information on ice crystal properties, remote-sensing technologies on board of satellites or long-range aircraft have to be applied.

The relative contribution of individual cloud layers to the overall retrieval of cloud properties from remote sensing was investigated by Platnick (2000). He found for vertically inhomogeneous liquid water clouds that the vertical weighting function (VWF) for cloud-top reflectivity measurements has a maximum at the cloud top layer with an optical thickness less than 2. The calculated VWFs strongly depend on solar zenith angle and the wavelength applied for the retrieval (1600 nm, 2200 nm or 3700 nm). The greater the absorption and the solar zenith angle, the larger is the maximum of the VWF and the closer this maximum is located to cloud top. These spectral differences in the VWFs at four different spectral bands of the Moderate Resolution Imaging Spectroradiometer (MODIS) were utilized by Chang and Li (2002, 2003) and recently by Chen et al. (2008) to estimate the vertical variation of cloud droplet effective diameter from remote sensing for liquid water clouds.

In this study we present a similar method to characterize the vertical distribution of ice crystals in ABM clouds. Airborne measurements of solar spectral cloud reflectivity and in situ data of cloud microphysical properties were utilized in combination with radiative transfer simulations. The measurements were performed during the Arctic Study of Tropospheric Aerosol, Clouds and Radiation (ASTAR) 2007 campaign in the vicinity of Svalbard (78° N, 15° E).

The instrumentation of the aircraft and the observations of spectral cloud-top reflectivity and microphysical properties are described in Sects. 2 and 3. The radiative transfer simulations combining in situ and remote-sensing measurements are discussed in Sect. 4. Subsequently, the vertical weighting function of remote-sensing measurements and the inferred evidence of ice crystals at cloud top are investigated in Sects. 5 and 6. Finally, visual observations of backscatter glories above the investigated clouds are discussed in Sect. 7.

2 Instrumentation

During ASTAR 2007 the POLAR 2 aircraft, owned by the Alfred Wegener Institute for Polar and Marine Research (AWI), Bremerhaven, Germany, was equipped to probe clouds with airborne remote-sensing and in situ instruments. The Airborne Mobile Aerosol Lidar (AMALi) and in situ instruments such as Polar Nephelometer, Cloud Particle Imager (CPI), and Particle Measuring System (PMS) Forward Scattering Spectrometer Probe (FSSP-100) have been described in detail by Lampert et al. (2009) and Gayet et al. (2009), respectively.

The study presented here analyzes data from the Spectral Modular Airborne Radiation measurement sysTem (SMART-Albedometer, Wendisch et al., 2001; Bierwirth et al., 2009). The specific configuration of the SMART-Albedometer operated during ASTAR 2007 has been

introduced in detail by Ehrlich et al. (2008a). It provides measurements of downwelling and upwelling spectral irradiances ($F_\lambda^\downarrow$, $F_\lambda^\uparrow$) simultaneously with upwelling nadir spectral radiance ($I_\lambda^\uparrow$). These data were used to calculate spectral cloud-top reflectivitys R in the wavelength range between 350 nm and 2150 nm by

$$R(\lambda) = \frac{\pi\, sr \cdot I_\lambda^\uparrow}{F_\lambda^\downarrow}. \quad (1)$$

In this definition $F_\lambda^\downarrow$ includes diffuse and direct solar radiation and is measured with respect to a horizontal plane $F_\lambda^\downarrow = F_\lambda^\downarrow(\cos\theta)$ with θ being the solar zenith angle. The spectral resolution of $R(\lambda)$ (full width at half maximum, FWHM) amounts to 2–3 nm in the wavelength range 350–950 nm and 9–16 nm for λ = 950–2150 nm wavelength.

3 Measurements

ABM clouds were observed during ASTAR-2007 (Ehrlich et al., 2008a; Gayet et al., 2009) above the Greenland Sea. Cold air outbreaks with northerly winds initiated extended boundary-layer cloud fields. The convection above the relatively warm open sea allowed the coexistence of ice and liquid water in these clouds.

We focus on measurements conducted on 7 April 2007. In situ measurements are obtained from two subsequent ascents and descents each of about 6 min duration. The cloud-top reflectivity measurements have been conducted on the same flight track about 10 min later. The horizontal leg was performed at 1770 m altitude which was about 150 m above cloud top. For this short time delay, advection can be neglected considering the wide cloud field as shown by satellite images. The reflectivity data have been averaged over a time period of about 18 min. The temporal variation of the data did not show a significant change of the cloud characteristics. The data collected on this day have already been analyzed with regard to their thermodynamic phase in Ehrlich et al. (2008a). During that day mixed-phase clouds were found to be dominant as revealed by both in situ measurements and SMART-Albedometer data.

3.1 In situ measurements

In situ measurements of microphysical and optical properties of the observed clouds have been presented by Ehrlich et al. (2008a). Mixed-phase clouds with similar properties observed during ASTAR 2007 on 9 April are investigated by Gayet et al. (2009) including a detailed discussion of measurement uncertainties of the in situ probes applied here.

The vertical profiles of particle number concentration, ice and liquid water content (IWC, LWC) and volumetric asymmetry parameter $\langle g \rangle$ obtained on 7 April 2007 are given in Fig. 1 (similar to Fig. 2 in Ehrlich et al., 2008a). Similar to

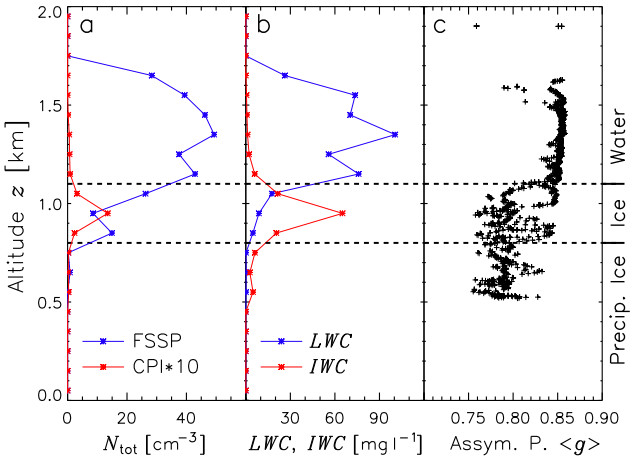

Fig. 1. Profiles of microphysical measurements obtained on 7 April 2007 (partly identical to Fig. 2 in Ehrlich et al., 2008a). Total particle number concentration $N_{\rm tot}$ measured by FSSP and CPI are given in panel a; LWC and IWC in panel b. The volumetric asymmetry parameter $\langle g \rangle$ obtained from the Polar Nephelometer is shown in panel c.

observations by Gayet et al. (2009) on 9 April 2007, it was found that the upper cloud layer (1600–1200 m altitude) was dominated by liquid water droplets. This is indicated by the Polar Nephelometer measuring high asymmetry parameters ($\langle g \rangle$ = 0.83–0.86) which are typical for spherical liquid water droplets. The microphysical and optical properties of the liquid water droplets are summarized in Table 1. In total, liquid water droplets have been observed between 800–1600 m with an average LWC of 44 mg l^{-1} (maximum up to 240 mg l^{-1}) and a droplet effective diameter of 15 µm. This corresponds to a liquid water path LWP of 35 g m^{-2} (LWP = LWC·Δz). The fractional liquid water optical thickness $\tau_{\rm W}$ was calculated from the volumetric extinction coefficient $b_{\rm ext}$ obtained from in situ data ($\tau = b_{\rm ext} \cdot \Delta z$) and amounts to $\tau_{\rm W} = 7.5$.

The lower cloud part (800–1200 m altitude) contained a significant amount of ice mass with an IWC of 43 mg l^{-1} (maximum up to 200 mg l^{-1}). CPI measurements showed that irregular crystals were the dominant shape in all cloud layers. Ice water path IWP, fractional ice optical thickness $\tau_{\rm I}$ and ice crystal effective diameter $D_{\rm eff}^{\rm I}$ amount to IWP = 17 g m^{-2}, $\tau_{\rm I} = 0.5$ and $D_{\rm eff}^{\rm I} = 103$ µm.

Ice crystals and liquid water droplets together result in a total cloud optical thickness $\tau = \tau_{\rm W} + \tau_{\rm I} = 8$ and a total water path TWP of 52 g m^{-2}. Ice volume fraction $f_{\rm I}$=IWP/TWP and ice optical fraction $f_{\rm I}^* = \tau_{\rm I}/\tau$ derived for the entire cloud amount to 0.33 and 0.06, respectively.

Below 800 m altitude, precipitating ice crystals have been observed down to the surface by CPI and visual on-board observations.

A detailed discussion on potential sources of error of in situ measurements in mixed-phase conditions is given by Gayet et al. (2009) for observations similar those presented

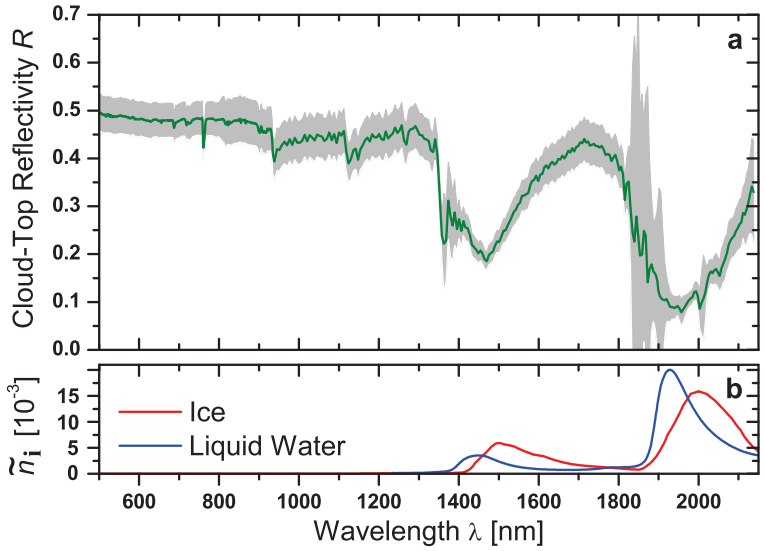

Fig. 2. Measured spectral cloud-top reflectivity R for ABM clouds observed on 7 April 2007. The measurement uncertainty is illustrated by the gray area. In Panel b shows the refractive index $\tilde{n}_i$ of liquid water (Wieliczka et al., 1989) and ice (Warren and Brandt, 2008).

Table 1. Microphysical and optical properties of the ABM cloud observed on 7 April 2007 (Case A0). For the closure study the cloud was divided into two sublayers, 800–1200 m and 1200–1600 m for which liquid water is situated in both layers. The adjusted values are used in the simulations of Case A where the cloud optical thickness was scaled to the observed cloud-top reflectivity.

			Measured Case A0	Scaled Case A
Liquid water	τ_W		7.5	16.9
800–1600 m	LWP	[g m^{-2}]	34.7	78.0
	LWC	[mg l^{-1}]	43.4	97.5
	D_{eff}^{W}	[µm]	14.8	14.8
Ice	τ_I		0.5	1.1
800–1200 m	IWP	[g m^{-2}]	17.2	38.7
	IWC	[mg l^{-1}]	42.5	96.8
	D_{eff}^{I}	[µm]	102.7	102.7
Total	τ		8.0	18.0
800–1600 m	TWP	[g m^{-2}]	51.9	116.7
	f_I^*		0.06	0.06
	f_I		0.33	0.33

here. By comparison of Polar Nephelometer measurements with scattering phase functions calculated from FSSP-100 cloud droplet size distributions it was found that shattering of ice crystals is low in liquid-dominated cloud layers due to low concentrations of large ice crystals ($D>100\mu$ m). In ice-dominated layers with higher concentrations of large ice crystals the measured LWC could likely be overestimated due to shattering. Subsequently, the above given values of

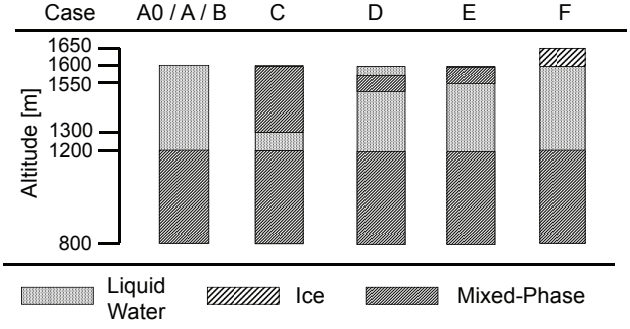

Fig. 3. Cloud geometries as used in the radiative transfer simulations for the cases A–F and for the simulations using the measured cloud properties (Case A0).

f_I and f_I^* might be biased, which will be addressed in Section 4.2.

3.2 Cloud-top reflectivity measurements

The spectral cloud-top reflectivity measured above the observed cloud is shown in Fig. 2a with its measurement uncertainty indicated by the gray area. These data have already been presented by Ehrlich et al. (2008a, Fig. 3). Below 1300 nm wavelength R is almost independent of wavelength except for water vapor ($\lambda = 920$ nm and $\lambda = 1130$ nm) and oxygen absorption bands ($\lambda = 762$ nm). At longer wavelengths water vapor absorption is stronger (1350–1500 nm and 1800–1950 nm) which significantly increases the measurement uncertainties in these spectral ranges.

The properties of cloud particles like concentration and effective diameter strongly alter the cloud-top reflectivity. In

general a higher particle concentration is linked to a higher cloud optical thickness and increases R almost independently of wavelength. The particle effective diameter is an indirect measure of the fraction of radiation which is absorbed by clouds. The larger the effective diameter of the particles, the higher is the absorbed fraction and the lower is R. Absorption due to the different cloud particles (hereinafter called liquid water and ice absorption) is superimposed on R in the spectral range above 1300 nm wavelength. This is indicated by the imaginary part of the refractive indices $\tilde{n}_i$ of liquid water and ice in Fig. 2b. The local minima of the measured R at $\lambda = 1490$ nm and $\lambda = 1950$ nm coincide with the maxima of $\tilde{n}_i$ (maximum absorption by cloud particles). These spectral features in the data have been analyzed by Ehrlich et al. (2008a) to identify the cloud thermodynamic phase with two different ice indices. The ice indices weight the ice and liquid water absorption present in the spectral reflectivity measurements. The spectral slope of R in the wavelength range between 1550 nm and 1700 nm is utilized in the spectral slope ice index I_S. Principle components related to ice and liquid water absorption are compared in the principle-components ice index I_P. For pure liquid water clouds, values of $I_S < 20$ and $I_P < 1$ are obtained. Strong ice absorption increases the spectral features in R and increases both ice indices.

Ehrlich et al. (2008a) stated that these phase-discriminating spectral features are most sensitive to upper cloud layers. The cloud-top reflectivity presented here leads to values of $I_S = 30$ and $I_P = 2.3$. Considering the observed vertical structure of ABM clouds with liquid water dominating the cloud top, the ice indices derived for these clouds range slightly above values expected for clouds with a liquid cloud top layer ($I_S < 20$ and $I_P < 1$).

Therefore, we have applied the measured microphysical and radiative cloud properties in spectral radiative transfer simulations with focus on the vertical structure of ABM clouds.

4 Simulated cloud-top reflectivity

Solar spectral radiative transfer simulations are performed with the libRadtran (Library for Radiative transfer) code by Mayer and Kylling (2005) for the wavelength range from 300 nm to 2200 nm adapted to the spectral resolution of the SMART-Albedometer. For the one-dimensional (1-D) simulations the discrete ordinate solver DISORT version 2.0 by Stamnes et al. (1988) is applied. The meteorological input is similar to radiative transfer simulations presented by Ehrlich et al. (2008a). Profiles of static air temperature, relative humidity and static air pressure are obtained from a radio sounding at Ny-Ålesund/Svalbard (7 April 2007, 11:00 UTC). Corresponding to the observed marine clouds, the spectral surface albedo is represented by measurements above sea water obtained on 7 April (Ehrlich, 2009).

Spectral cloud optical properties (extinction coefficient, single scattering albedo and scattering phase function) have been calculated from optical properties of individual cloud particles. Mie theory is applied for liquid water droplets. Ice particles have been assumed to be column-shaped crystals. The optical properties of columns are provided by Yang and Liou (1996). Columns do not perfectly suit the CPI measurements which mostly identified irregular crystals in the clouds. However, for the simulations presented here the choice of particle shape is less important than the ice crystal effective diameter. The impact of ice crystal shape on the radiative transfer in mixed-phase clouds has been evaluated by Ehrlich et al. (2008b). They found that liquid water droplets dominate the cloud optical properties. Ice crystal shape effects are significant only for the presence of small ice crystals, $f_I > 0.5$ and if the IWC is kept constant when changing the ice crystal shape. For ice crystals of a size similar to that observed in this study (D^I_{eff}=103 µm), shape effects are lower than 1% for cloud reflectivity and transmittivity. For cloud absorptivity which is relevant in this study the simulations by Ehrlich et al. (2008b) showed no measurable shape effect at all. This indicates that in the wavelength range where ice absorption occurs, the predetermined effective diameter of cloud particles characterizes the absorption independent of particle shape. Furthermore, for the reflectivity at visible wavelengths where absorption by cloud particles is negligible the scattering phase function characterizes the scattering processes. However, the part of the ice crystal scattering phase function relevant for the solar zenith angle used in the simulation ($\theta_0 = 71°$) is similar for different ice crystal shapes.

4.1 Cloud optical thickness

Based on the in situ measurements the cloud was divided into two vertical sublayers representing the observed vertical structure of the clouds. The upper cloud layer (1200–1600 m) contains only liquid water droplets, whereas the lower cloud layer (800–1200 m) contains both liquid water droplets and ice crystals. The assumption of a pure liquid upper cloud layer is justified by the optical thickness of the ice crystal population measured by the CPI which was less than 0.03. Simulations not shown here reveal that this low ice concentration alters the cloud reflectivity by less than 0.2 % which is far below the measurement uncertainties. Thus ice crystals in the upper cloud layer are neglected in the following simulations. Figure 3 illustrates the cloud model used for the radiative transfer simulations (Case A0). The microphysical and optical properties of each layer are given in Table 1.

4.1.1 Unscaled

The cloud-top reflectivity R simulated with the measured cloud optical properties (Case A0) is compared in Fig. 4a to measurements of R (dashed black and green solid lines). The

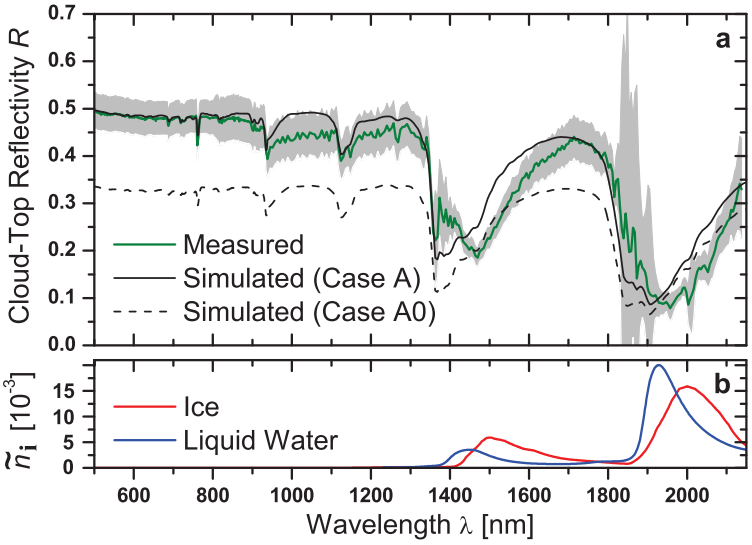

Fig. 4. Simulated (Cases A0 and A) and measured spectral cloud-top reflectivity R (panel a). The measurement uncertainty is illustrated by the gray area. In Panel b shows the refractive index $\tilde{n}_i$ of liquid water (Wieliczka et al., 1989) and ice (Warren and Brandt, 2008).

measurement uncertainty of R is indicated by the gray area. Especially at wavelengths shorter than 1800 nm the simulations (dashed line) range below the measured R and are outside the measurement uncertainties. This indicates that the cloud optical thickness is underestimated by the in situ measurements.

Beside uncertainties of the in situ instruments, cloud inhomogeneities cause problems for deriving representative cloud optical properties. During the in situ probing several areas with low particle concentrations and low extinction coefficients b_{ext} were sampled related to the undulating structure of the observed clouds. By averaging the measurements over the total time when the Polar Nephelometer measured considerable amounts of cloud particles ($b_{ext} > 0.05\,km^{-1}$) the mean values of b_{ext} underestimate the total cloud optical thickness. Maximum values of $b_{ext} = 35\,km^{-1}$ and $b_{ext} = 20\,km^{-1}$ have been measured for liquid water droplets by FSSP and Polar Nephelometer, respectively. In the thin ice layer the extinction coefficient of the ice crystal population amounts up to $b_{ext} = 13\,km^{-1}$ as measured by the CPI. The underestimation of the cloud optical thickness due to cloud inhomogeneities can be reduced by an extended sampling time of the cloud. During ASTAR 2007 the clouds have been probed during descents and ascents of the POLAR 2 with climbing rates of $200\,m\,min^{-1}$ which reduces the sampling time for individual vertical cloud layers even more.

4.1.2 Scaled

In order to adjust the results of the radiative transfer simulations to the measured R in the wavelength range $\lambda < 1800$ nm the cloud optical thickness is scaled in the following simulations. Therefore, the total liquid water droplet and ice crystal concentrations are varied. The scaling was applied by keeping cloud particle effective diameter, f_I^*, and f_I unchanged. Microphysical and optical properties of the scaled cloud (hereafter referred as Case A) are given in Table 1. With $\tau = 18$ the scaled total cloud optical thickness is more than doubled compared to the values derived from the in situ measurements.

The results of the radiative transfer simulations for Case A are shown in Fig. 4a as a solid black line. For wavelengths less than 1400 nm the simulated R ranges within the measurement uncertainties. However, at wavelengths where ice absorption is strong, as indicated by the imaginary refractive index displayed in Fig. 4b, the simulated R is higher than measured. This reveals that in the model cloud ice crystals are too small or less ice crystals are present than indicated by the remote-sensing measurements.

It has to be pointed out that the large factor between τ derived from in situ measurements and τ derived from the reflectivity measurements is reduced when the uncertainties of the SMART-Albedometer are considered. Fitting the simulations to the lower boundary of the uncertainty range in wavelengths below 1400 nm (not shown here) yields $\tau = 12$. However, further simulations have shown that the spectral signature in the wavelength range of strong ice absorption and thus the investigations shown below are not significantly affected by the optical thickness of the cloud.

As shown by Ehrlich et al. (2008a), the spectral slope ice index I_S and the principle-components ice index I_P obtained for this particular cloud are $I_S = 30$ and $I_P = 2.3$, respectively. From the simulated cloud-top reflectivity (Case A) values of $I_S = 13.4$ and $I_P = 0.7$ were calculated. These values are in the range which is derived for pure liquid water

Table 2. Microphysical and optical properties of ABM clouds for cases B1–B6 characterized by different ice optical fractions f_I^*. The total cloud optical thickness is scaled to gain a cloud-top reflectivity similar to the observations for $\lambda < 1300$ nm.

			B1	B2	B3	B4	B5	B6
Liquid Water	τ_W		18.0	16.2	14.0	9.6	6.0	0.0
800–1600 m	LWP	[g m^{-2}]	83.0	74.7	64.6	44.3	27.7	0.0
	LWC	[mg l^{-1}]	103.8	93.4	80.8	55.4	34.6	0.0
Ice	τ_I		0.0	1.8	3.5	6.4	9.0	10.8
800–1200 m	IWP	[g m^{-2}]	0.0	61.4	119.3	218.2	306.9	306.9
	IWC	[mg l^{-1}]	0.0	153.5	298.3	545.5	767.3	767.3
Total	τ		18.0	18.0	17.5	16.0	15.0	10.8
800–1600 m	TWP	[g m^{-2}]	83.0	136.1	183.9	262.5	334.6	306.9
	f_I^*		0.00	0.10	0.20	0.40	0.60	1.00
	f_I		0.0	0.45	0.65	0.83	0.92	1.00

clouds, which is not surprising as the ice optical fraction $f_I^* = 0.06$ of the simulated cloud is close to zero. The uncertainties of the measured f_I^* deduced from the simultaneous FSSP and CPI measurements are addressed in the following section.

4.2 Ice optical fraction

Based on the measured and scaled cloud optical properties of Case A the ice optical fraction f_I^* was varied between values corresponding to pure liquid water clouds ($f_I^* = 0.0$) and a pure ice cloud ($f_I^* = 1.0$). Microphysical and optical properties of the six simulated clouds with different ice optical fraction referred as Case B1–B6 are given in Table 2. Cloud geometry and particle effective diameter D_{eff}^w, D_{eff}^I are identical to cloud Case A. Due to differences in the scattering phase function of liquid water droplets and ice crystals, the cloud-top reflectivity increases with increasing f_I^* if the total cloud optical thickness is kept constant. In order to fit R in the wavelength range $\lambda < 1300$ nm to the measured values, the total cloud optical thickness of Case B1–B6 was scaled separately for each cloud.

The results of the radiative transfer simulations are given in Fig. 5a. All simulations range between two extreme cases; the pure liquid water cloud (B1, blue line) and the pure ice cloud (B6, red line). Corresponding ice indices I_S and I_P calculated from the simulations are listed in Table 3. The comparison with the measured ice indices indicates that the simulated cloud Case B5 with $f_I^* = 0.6$ fits best to the measurements.

However, in Fig. 5a the analysis of the spectral structure of R in the wavelength range dominated by ice and liquid water absorption between 1400 nm and 2150 nm reveals that none of the simulated cases match the measurements throughout the entire wavelength range. For low ice optical fractions $f_I^* < 0.4$ the ice crystal concentration is too low and the resulting ice absorption is too weak to reproduce the observed minima of R. These minima were present in the reflectivity measurements at 1490 nm and 2000 nm wavelengths which agrees with the maxima in the refraction indices of ice plotted in Fig. 5b. However, at wavelengths where ice absorption is weaker (1600–1800 nm) R is in the range of the measurement uncertainties of the measured R for $f_I^* < 0.4$. The opposite is obtained for simulations with $f_I^* \geq 0.4$. For these cases ice absorption is strong enough to reproduce the local minima in the reflectivity measurements. However, increasing ice absorption additionally reduces the cloud-top reflectivity at wavelengths between 1600 nm and 1800 nm. In this wavelength range the simulations with $f_I^* \geq 0.4$ fail to fit the measured R.

Table 3. Spectral slope ice index I_S and principle-component ice index I_P for the simulations of the clouds cases B1–B6. Additionally the values obtained from the SMART-Albedometer measurements are given.

	B1	B2	B3	B4	B5	B6	Measured
I_S	11.4	14.3	16.2	20.4	26.9	56.2	29.8
I_P	0.5	0.8	1.0	1.5	2.2	5.0	2.3

It seems that there has to be another parameter which alters the spectral slope in the wavelength range dominated by ice and liquid water absorption (1400–2200 nm). From additional radiative transfer simulations using modified cloud models (not shown here) it was found that neither the particle effective diameter of the ice crystals and liquid water droplets nor the ice crystal shape are responsible for the observed spectral pattern of R. Therefore, in the following section the vertical weighting function (VWF) of the cloud-top reflectivity measurement is investigated.

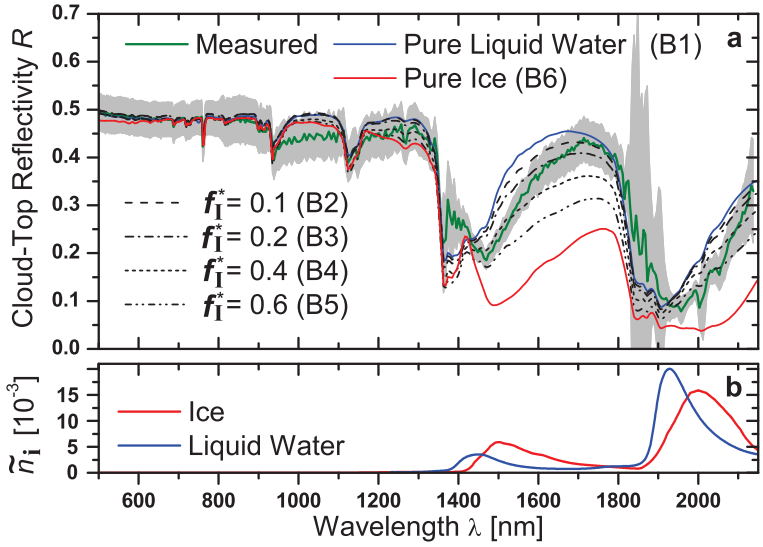

Fig. 5. Measured spectral cloud-top reflectivity R and simulated R for mixed-phase clouds of different f_I^* (Case B1–B6). The measurement uncertainty is illustrated by the gray area. In Panel b shows the refractive index $\tilde{n}_i$ of liquid water (Wieliczka et al., 1989) and ice (Warren and Brandt, 2008).

5 VWF of reflectivity measurements

We applied the methods described by Platnick (2000) to characterize the vertical weighting of the reflectivity measurements in the wavelength range dominated by ice and liquid water absorption (1300–1800 nm).

Platnick (2000) proposed to use the maximum vertical photon penetration as VWF of R. It is argued that in a cloud of optical thickness τ_C the fraction P_{ref} of all reflected photons that penetrate to a maximum depth between τ and $\tau+\Delta\tau$ is represented by

$$P_{\text{ref}}(\tau) = \frac{R(\tau+\Delta\tau) - R(\tau)}{R(\tau_C)}. \quad (2)$$

Here $R(\tau)$ is the reflectivity from the portion of the cloud above the level $\tau = \tau(z)$ (i.e., calculated for a cloud layer between cloud top and $\tau(z)$ with lower layers absent). Normalizing with $\Delta\tau$ the vertical weighting function $w(\tau)$ is

$$w(\tau) = \frac{R(\tau+\Delta\tau) - R(\tau)}{R(\tau_C)} \cdot \frac{1}{\Delta\tau}. \quad (3)$$

To obtain a VWF $W(z)$ in units of [% m^{-1}] referring to the geometrical thickness of the cloud, we converted $w(z)$ considering that $\Delta\tau = b_{\text{ext}}(z) \cdot \Delta z$. By multiplying $w(z)$ by the vertical profile of the extinction coefficient $b_{\text{ext}}(z)$ we obtain

$$W(z) = w(z) \cdot b_{\text{ext}}(z) \cdot 100\%. \quad (4)$$

Thus $W(z)$ gives the percentage contribution of each cloud layer to the radiance observed above cloud top.

The vertical profile of the cloud-top reflectivity R used to calculate $W(z)$ is obtained from radiative transfer simulations similar to those presented in Sect. 4. The input for the cloud layer is identical to Case A matching the observed R at VIS wavelengths. According to the method described by Platnick (2000), the surface reflectivity was set to zero. Thus no multiple reflections between the surface and the cloud layer occur in the simulations which ensures that $W(z)$ is normalized between cloud base z_{base} and cloud top z_{top} by

$$\int_{z_{\text{base}}}^{z_{\text{top}}} W(z)\,dz = 1. \quad (5)$$

As discussed by Platnick (2000) for a low surface albedo (measurements during ASTAR have shown values below 0.05 above open ocean), this assumption has no significant impact on $W(z)$. With the same argumentation, aerosol which also scatters/reflects radiation below cloud base was excluded from the simulations.

The calculated $W(z)$ for two wavelengths exemplary for strong ice (1510 nm) and liquid absorption (1710 nm) are given in Fig. 6a. In Fig. 6b $W(z)$ is accumulated over altitude starting with 0% at cloud top. For both wavelengths the weighting shows the highest contribution for cloud layers close to cloud top at 1550 m altitude. The maximum values of $W(z)$ are found to be higher for $\lambda = 1510$ nm than for $\lambda = 1710$ nm. With the higher values of $W(z)$ the cloud-top reflectivity at $\lambda = 1510$ nm is dominated stronger by absorption by particles at cloud top than R at $\lambda = 1710$ nm. Therefore, R at $\lambda = 1510$ nm is more suitable to retrieve the particle size at cloud top.

A decrease of $W(z)$ with increasing cloud depth is observed for both wavelengths. The accumulated weighting (Fig. 6b) shows that 50% of the measured signal at 1710 nm wavelength emanates from the cloud layer above 1410 m.

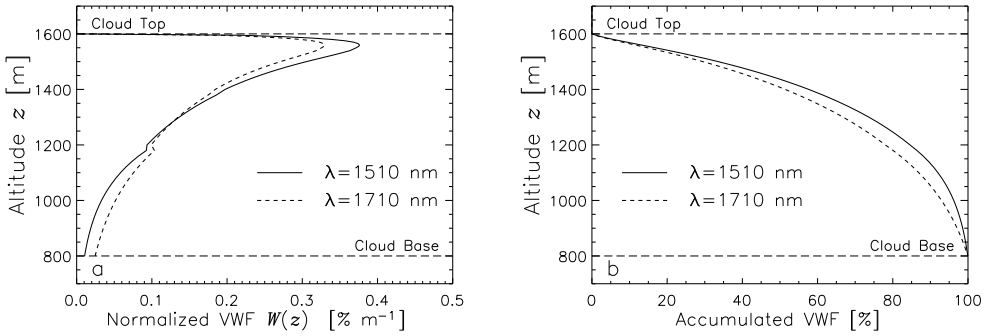

Fig. 6. Vertical weighting function $W(z)$ for the radiance measurements of the SMART-Albedometer with respect to absorption by the cloud particles using the cloud Case A (panel a). The accumulated weighting is given in panel b.

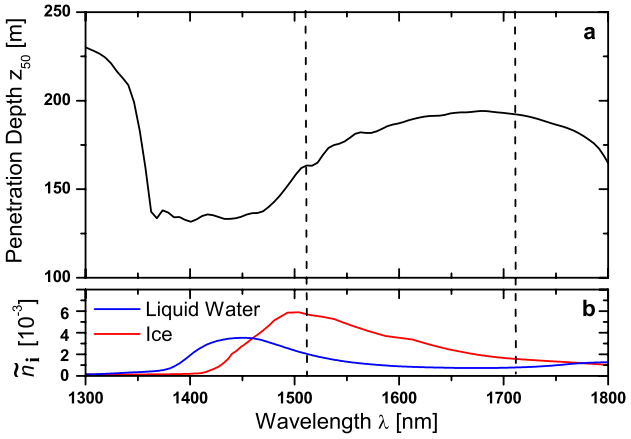

Fig. 7. Characteristic photon penetration depth characterizing the upper cloud layer related to 50% of the measured signal (panel a). In panel b the refractive index $\tilde{n}_i$ of liquid water (Wieliczka et al., 1989) and ice (Warren and Brandt, 2008) is displayed.

Only 10% correspond to the cloud layer below 1060 m. For $\lambda = 1510$ nm a steeper slope is obtained (50% at 1440 m).

In this way a characteristic photon penetration depth z_{50} is determined for all wavelengths. It specifies the depth of the cloud layer (measured from cloud top) which is related to 50% of the measured reflectivity signal. z_{50} is shown in Fig. 7 for the wavelength range 1300–1800 nm. The spectral differences of z_{50} are mostly due to absorption of radiation within the cloud. At wavelengths dominated by water vapor absorption ($\lambda = 1350$–1500) the minimum of z_{50} with values below 150 m is obtained. Between 1500 nm (high ice absorption) and 1700 nm (low ice absorption) z_{50} increases from about 160 m to 195 m. This supports the assumption that the observed absorption signal in the radiance measurements for $\lambda = 1490$ nm emanates from layers close to cloud top while the absorption observed at longer wavelengths about 1710 nm includes particles located at lower cloud layers.

These spectral differences in the VWF provide a tool to retrieve information on the vertical distribution of the cloud particle effective diameter, as described by Chen et al. (2007). In contrast to Chen et al. (2007) the investigations shown here are limited to a small wavelength range (1400–1800 nm). However, this range includes one spectral maximum and one spectral minimum of ice and liquid water absorption and is covered by the SMART-Albedometer measurements with sufficient spectral resolution to analyze these spectral differences. Wavelengths where liquid water and ice absorption are strong can be used to derive particle properties at cloud top, whereas wavelengths with weaker absorption give information on particles located at lower cloud layers. Utilizing the spectral differences between the maxima of ice and liquid water absorption, separate vertical profiles for ice crystals and liquid water droplets can be derived.

The measurements of R presented in Fig. 4a showed that for wavelengths below $\lambda = 1700$ nm stronger absorption is measured than shown by the simulations. The maximum differences overlap with the ice absorption maximum ($\lambda = 1490$ nm). At wavelengths between 1700–1800 nm weaker absorption is observed. Following the findings discussed above, the strong absorption at $\lambda = 1490$ nm implies that ice crystals of large effective diameter are present in the upper cloud layers. On the other hand, the high values of R between 1700–1800 nm wavelength indicate cloud particles with smaller effective diameter at cloud top and at lower cloud layers. This conclusion differs from the vertical distribution of ice crystals and liquid water droplets obtained by the in situ measurements presented here. This may explain the discrepancy between simulated and measured cloud-top reflectivity.

6 Ice crystals at cloud top

The analysis of the VWF calculated for the radiance measurements suggests that ice crystals might be present at cloud top of the clouds observed on 7 April. The question is where exactly the ice is situated. In general it can be read from the calculated VWF in Fig. 6a that all altitudes where $W(\lambda = 1510\,\text{nm})$ is higher than $W(\lambda = 1710\,\text{nm})$ are

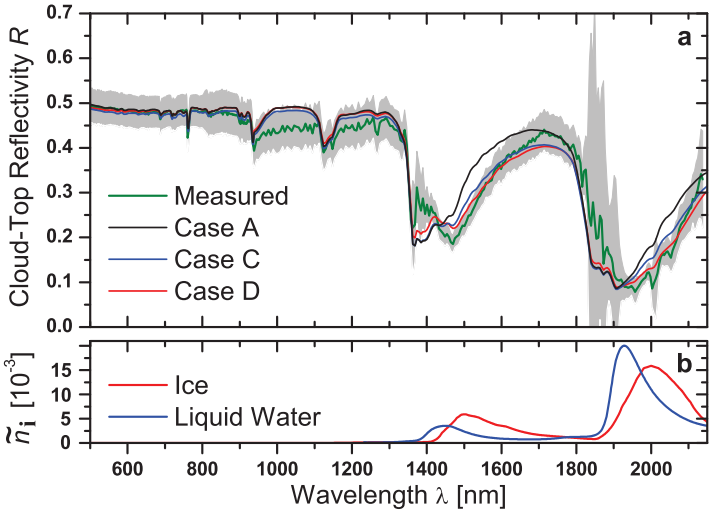

Fig. 8. Measured and simulated spectral cloud-top reflectivity R for cases A, C and D (panel a). The measurement uncertainty is illustrated by the gray area. In Panel b shows the refractive index $\tilde{n}_i$ of liquid water (Wieliczka et al., 1989) and ice (Warren and Brandt, 2008).

appropriate. At these altitudes the difference between the SMART-Albedometer sensitivity to ice ($\lambda = 1510$ nm) and liquid water absorption ($\lambda = 1710$ nm) are largest. Adding ice crystals here will reduce the simulated cloud-top reflectivity at $\lambda = 1510$ nm stronger than at $\lambda = 1710$ nm.

Therefore, the original cloud simulated with Case A was modified in Case C–F (Fig. 3) by adding ice crystals at cloud top. For Case C the ice is distributed over the entire altitude range (1300–1600 m) where $W(\lambda = 1510\,\text{nm})$ is higher than $W(\lambda = 1710\,\text{nm})$; in Case D the ice is concentrated in a thin layer 1525–1575 m where the differences in W are strongest. For Case E the thin ice layer is situated adjacent to cloud top within the original cloud (mixed-phase cloud top); for Case F a thin ice layer is added above cloud top as illustrated in Fig. 3. The optical thickness of the thin ice layer was set to 0.5 in all cases with ice crystal effective diameter similar to the ice layer at cloud base ($D_{\text{eff}}^{\text{I}} = 103\,\mu\text{m}$, column shape). Due to adding the ice layer, the total optical thickness of the cloud is adjusted to $\tau = 16.5$ for Case C, $\tau = 16.0$ for Case D, $\tau = 15.0$ for Case E and $\tau = 14.5$ for Case F.

The spectral cloud-top reflectivity R simulated for the cases C–F is shown in Figs. 8 and 9. In general, all cases show a better agreement with the measurements compared to the simulations presented above (cases A and B). For cases D–F which have almost identical results these simulations fit into the uncertainty range of the observed R at all wavelengths. Especially the spectral pattern in the wavelength range dominated by ice and liquid water absorption is closer to the measurements than simulations without additional ice layer. This reveals that ice crystals situated at cloud top are necessary to explain the observed absorption features with strong absorption at 1490 nm and weak absorption at wavelengths about 1750 nm. The simulations of Case C show a slight deviation at wavelengths of strong ice absorption ($\lambda \approx 1500$ nm and $\lambda \approx 2050$ nm) which indicates that Case C does suit the observed clouds less than Cases D–F. The ice crystals are more likely situated in the altitude range with the highest sensitivity of the reflectivity measurements (highest W at about 1550 m) than homogeneously distributed over a thicker layer. It has to be stated that this holds only for ice crystals of large effective diameter which if added describe the observed ice absorption in the measurements. Ice crystals of small effective diameter in low concentration which do not contribute as strongly to the ice absorption might be located throughout the cloud.

From the in situ measurements of the microphysical cloud properties no solid evidence of ice crystals in the uppermost cloud layer was found. Of all 69 measurements obtained by the Polar Nephelometer above 1500 m altitude, only 7 indicated ice crystals with asymmetry parameters below 0.82 (cf. Fig. 1). These measurements do not significantly alter the volumetric asymmetry parameter ($\langle g \rangle = 0.85$) calculated for this cloud layer. The CPI registered ice particles only at five times in the data analyzed here. The measured low ice concentration is probably caused by the short sampling time in this cloud layer which is limited due to performing ascents and descents into the cloud instead of horizontal legs at a fixed altitude. With a slightly varying cloud top height the ice crystals might not be represented well in the measurements. For individual profiles measured in the same cloud field but not included in the analysis shown here (due to their displacement to the remote sensing measurements) the CPI sampled several large ice crystals at cloud top with up to 500–800 μm maximum sizes. These ice crystals have been mostly rimed particles (graupel) but could not be found in all measured profiles. Furthermore, the horizontal variability

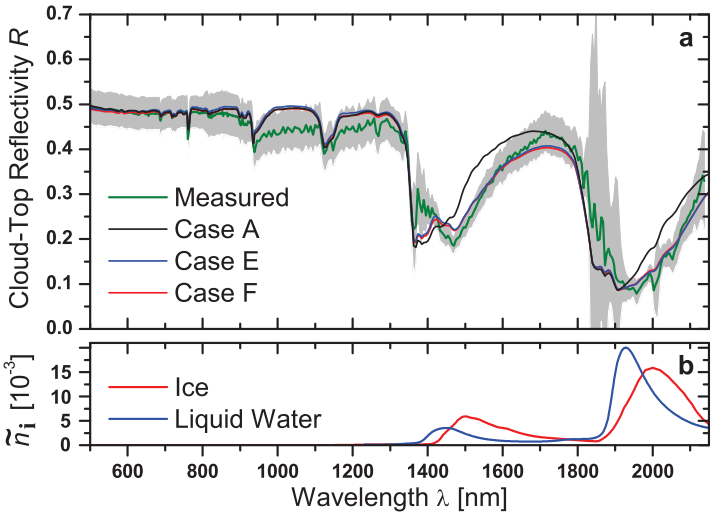

Fig. 9. Measured and simulated spectral cloud-top reflectivity R for cases A, E and F (panel a). The measurement uncertainty is illustrated by the gray area. In Panel b shows the refractive index $\tilde{n}_i$ of liquid water (Wieliczka et al., 1989) and ice (Warren and Brandt, 2008).

of ABM clouds as shown by Gayet et al. (2009) and the time delay between in situ and remote-sensing measurements may explain the different results of both methods.

In general it is expected that ice crystal size increases towards cloud base due to crystal growth and aggregation (McFarquhar et al., 2007). Contrarily, in the simulations presented here large ice crystals are assumed to be of same size at cloud top and cloud base. There are two reasons which might explain this discrepancy with large ice crystals at cloud top. First it has to be pointed out that the radiation measurements always refer to the effective diameter and not to the physical length of an ice crystal. As stated by McFarquhar and Heymsfield (1998) it is possible that ice crystals increase in size but the effective diameter remains almost constant because the shape of the crystals changed. Ice crystals with approximately spherical shape have a higher effective diameter (volume to cross section ratio) than ice crystals like plates or dendrites of the same maximum size. The few CPI images collected at cloud top showed mostly rimed particles for which the volume to cross section ratio is higher than for regular ice crystals observed at lower cloud layers. Additionally, cloud dynamics may lift large ice crystals toward cloud top. The free fall speed of graupel of 1 mm size is about $1\,\mathrm{m\,s^{-1}}$. Such a vertical wind speed is compatible with dynamical processes in such boundary layer clouds. Unfortunately vertical wind speed was not measured on the POLAR 2 aircraft. However, as shown by Shupe et al. (2008b) for similar clouds the large temperature difference between sea surface and cloud layer causes updrafts up to $2.5\,\mathrm{m\,s^{-1}}$. In updraft regions large ice crystals might be lifted again and distributed at cloud top. Further investigations exceeding the focus of this study will be necessary to address this hypothesis.

7 Simulation of the backscatter glory

The backscatter glory is an optical phenomenon based on single scattering processes and typical for spherical liquid water droplets. The intensity variations of the reflected radiation reflect the single scattering phase function of liquid water droplets located at cloud top. Therefore, the observations of backscatter glories have been used, e.g., by Gedzelman (2003); Mayer et al. (2004) to retrieve the cloud droplet effective diameter.

During the measurement flights of ASTAR 2007 backscatter glories have been observed frequently by eye and photo camera. The photographs have not been taken systematically. However, two exemplary photographs taken on 7 April, 11:05 UTC (78° N, 11.5° E) and 10 April, 11:31 UTC are shown in Fig. 10. The ice indices measured above these clouds ($I_S = 26.0/26.3$ and $I_P = 1.9/2.9$) are slightly lower than for the cloud for which the closure study is conducted. However, the values are higher than expected for pure liquid water clouds ($I_S < 20$ and $I_P < 1$) and indicate the presence of ice crystals at the same time the glories have been observed.

The presence of ice crystals at cloud top of the observed clouds was also concluded in Sect. 6. However, the observations of the backscatter glory put this finding into question as the scattering phase function $\mathcal{P}(\vartheta)$ of ice crystals does not exhibit this feature. Figure 11 shows an extract of $\mathcal{P}(\vartheta)$ of ice crystals (columns) and liquid water droplet populations used in the simulations analyzed above. Displayed are three wavelengths $\lambda = 450$ nm, $\lambda = 550$ nm and $\lambda = 600$ nm representative for the blue, green and red color of the visible solar radiation.

For ice crystals $\mathcal{P}(\vartheta)$ increases with increasing scattering angle over the range of scattering angles considered (Fig. 11a). This is related to the large particle size of

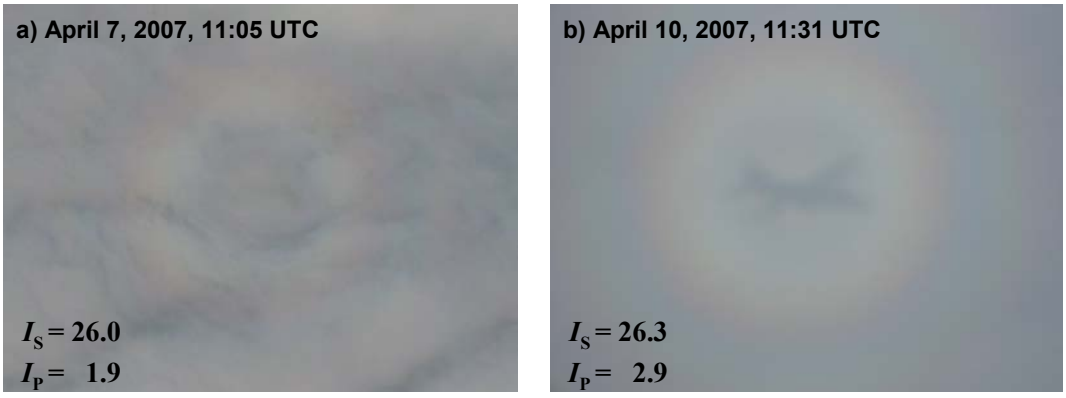

Fig. 10. Photographs of backscatter glories at cloud top. The left photograph was taken from the POLAR 2 aircraft on 7 April, 11:05 UTC, the right on 10 April, 11:31 UTC. The given ice indices I_S and I_P are derived from the SMART-albedometer measurements above these clouds (Ehrlich et al., 2008a).

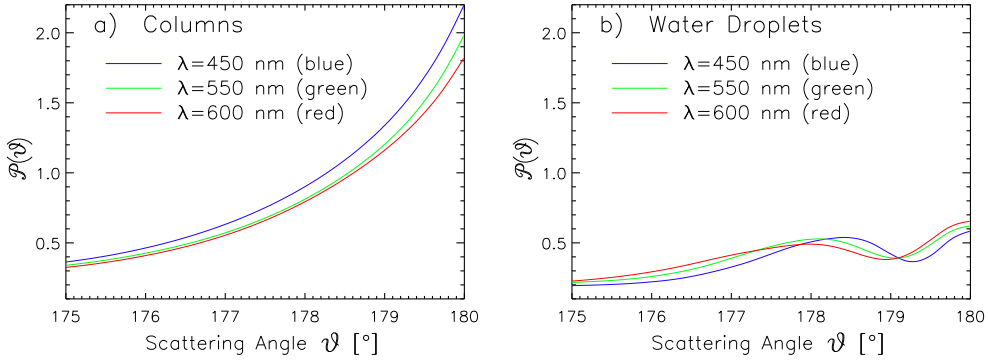

Fig. 11. Scattering phase function $\mathcal{P}(\vartheta)$ at three different wavelengths representative for the blue (450 nm), green (550 nm) and red (600 nm) color. The backscattering range between scattering angles $\vartheta = 175$–$180°$ is shown. In panel a $\mathcal{P}(\vartheta)$ is given for the ice crystal population (columns), in panel b for the liquid water droplet population used in the simulations.

$D^{I}_{eff} = 103\,\mu m$. The larger the particle size, the higher the backscattering ($\vartheta = 180°$) which is mainly caused by specular reflection at the ice crystal surface. In addition to the maximum at $\vartheta = 180°$ liquid water droplets (Fig. 11b) have a slight secondary maximum of $\mathcal{P}(\vartheta)$ at about $\vartheta = 178°$ for 550 nm and 600 nm wavelengths and at about $\vartheta = 178.5°$ for 450 nm. This second maximum causes the increased intensity of reflected radiation observed on the glory phenomena. The shift of the maximum for the different wavelengths produces the color dispersion of the glories.

3-D Monte Carlo simulations have been performed to simulate the backscatter glory. Applying the methods presented by Mayer and Emde (2007) the angular distribution of radiation scattered into the backscatter range $\vartheta \geq 175°$ was calculated. Considering the solar zenith angle of 71° this corresponds to viewing zenith angles between 71° and 76°. For the 3-D radiative transfer simulations the MYSTIC code (Monte Carlo code for the physically correct tracing of photons in cloudy atmospheres) embedded in the *libRadtran* package was applied (Mayer, 1999, 2000, 2009). With MYSTIC the backscattered radiance was calculated for the flight altitude of 1800 m approximately 200 m above cloud top. In the simulations the extension of the solar disk of 0.5° is considered. Therefore, the radiance distribution is convoluted with $\sqrt{\theta_S^2 - (\theta - \theta_0)^2}$ where θ_0 is the solar zenith angle specified for the center of the solar disk and θ_S the angular radius of the solar disk. The convolution causes a slight smoothing of the resulting radiance distribution which is not essential for the conclusions presented here but large enough to be considered.

Finally, the radiances were converted to color (R,G,B) values following the procedure recommended by the Commission Internationale de l'Éclairage (CIE, CIE, 1986). The procedure is implemented in the C program *specrend.c* provided by CIE which was applied here (http://www.fourmilab.ch/documents/specrend/).

The angular distribution of the R,G,B colors was calculated for the three clouds cases A, E and F. Values of R,G,B normalized by the value at the backscattering angle $\vartheta = 180°$ are shown in the left panels of Fig. 12 for a viewing geometry

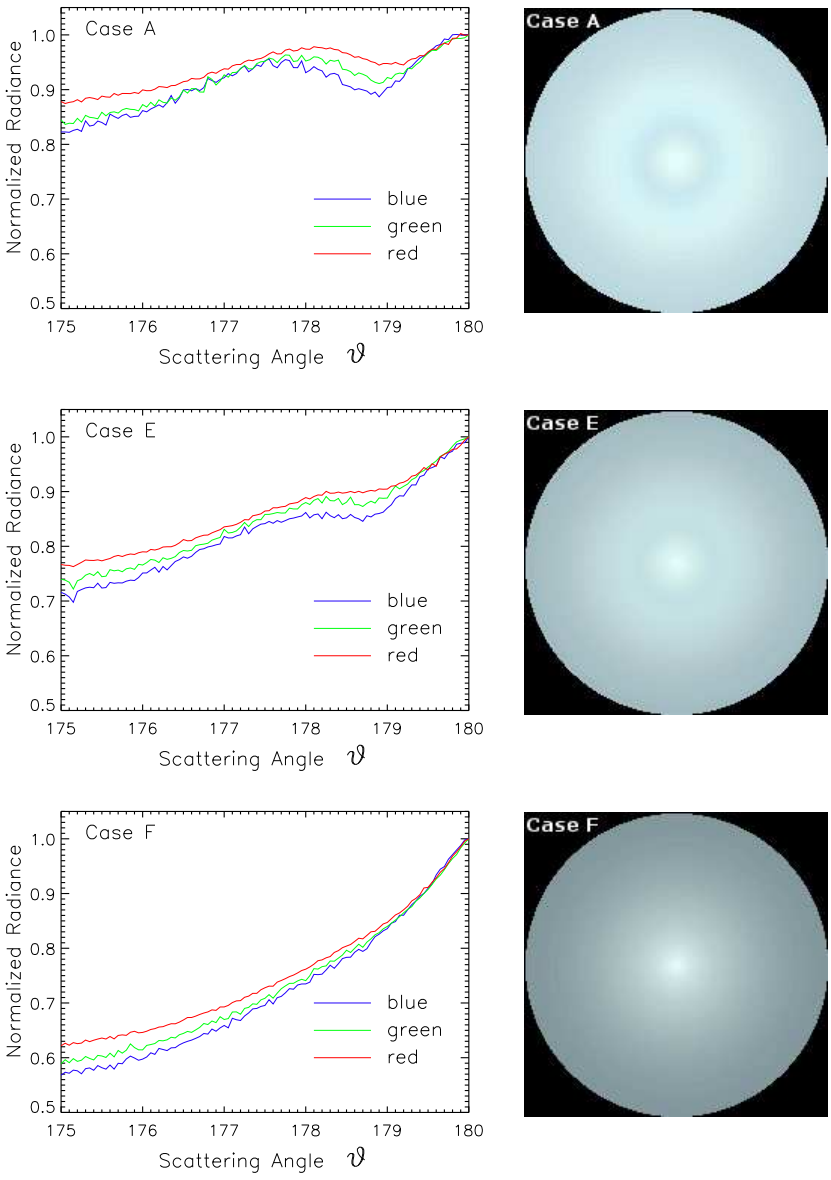

Fig. 12. Radiative transfer simulations of the angular distribution of spectral radiances of the backscattering region. Results are shown for the three cases A, E and F. The left panels show the angular distribution converted into R,G,B colors. The visualization of the glory is given in the right panels.

with the Sun in the back. The right panels show R,G,B images of the modeled glory, obtained by rotating the angular distributions shown in the left panels. The rotation of the simulations is justified as additional simulations showed that the glory is symmetrical to the backscattering angle. In the results simulated for the cloud dominated by liquid water at cloud top (Case A) the backscatter glory is visible. Although the simulations exhibit some noise, the normalized radiance reflects the scattering phase function of liquid water droplets (cf. Fig. 11). The noise is due to the number of photons used in the Monte Carlo radiative transfer simulations but is not essential for the conclusions presented here. The wavelength shift of the secondary maximum is only weak in the simulations which results in the almost white color of the rotated image. This is due to the broad number size distribution of the liquid water droplets at cloud top used in the simulations. As shown by Mayer and Emde (2007) the colors of the backscatter glory are less pronounced if broad droplet size distributions are used. These findings are contrary to the glory photographs presented in Fig. 10 but may result from the differences of the location of the in situ measurements and the location where the photographs were taken.

For Case E where an ice layer of $\tau = 0.5$ is situated inside the uppermost cloud layer the backscatter glory is weaker

than in Case A, but still visible in the rotated R,G,B image. Close to the backscattering angle the radiance is higher than in Case A. This spot is caused by enhanced backscattering by the ice crystals. In airborne observations this spot is covered by the shadow of the aircraft and hence is unobservable. These results show that ice crystals of an optical thickness less than 0.5 situated inside the liquid water layer (mixed-phase cloud top, Case E) can reproduce the simultaneous observation of ice absorption and glory phenomena. The same holds for Case C and D (not shown here) where the uppermost cloud layer is less affected by ice crystals due to the different cloud geometries. Thus a more pronounced glory is obtained compared to Case E.

Contrarily, in Case F where the same ice layer is located above the liquid water layer the backscatter glory was not reproduced by the simulations. The angular distribution of the radiance shows similar characteristics as the scattering phase function of the ice crystals (cf. Fig. 11). From this analysis it is concluded that Case F does not suit the remote-sensing observation above ABM clouds obtained during ASTAR 2007.

8 Conclusions

Airborne measurements of cloud-top reflectivity R obtained during the ASTAR 2007 campaign have been analyzed to retrieve information on the vertical distribution of ice crystals in ABM clouds. For this purpose, spectral radiative transfer simulations of R are performed and compared to measured R. The radiative transfer simulations based on the microphysical properties obtained from in situ measurements during ASTAR 2007 (Case A0) underestimate R over the entire wavelength range by a factor of 1.5. This indicates that the cloud optical thickness is underestimated by the in situ measurements probably because of cloud inhomogeneities which bias the averaged cloud microphysical properties. With scaled cloud optical thickness (Case A) the radiative transfer simulations still failed to reproduce the spectral pattern of R observed in the wavelength range dominated by ice and liquid water absorption (1500–1800 nm). Varying the ice optical fraction (Case B1–B6) did not improve the results significantly.

Agreement within the measurement uncertainties between measurements and simulations was obtained when an ice layer of $\tau = 0.5$ was added in the simulations at cloud top where the reflectivity measurements are most sensitive to ice absorption (Cases C–F). This suggests that ice crystals were present in the upper layers of the observed clouds. Analysis of the in situ measurements could neither confirm nor reject these results. In general these data showed a cloud top dominated by liquid water droplets whereas ice crystals are dominant at lower cloud levels similar to the observation by Gayet et al. (2009). The absence of ice crystals in the in situ measurements at cloud top is probably due to the flight strategy (vertical profiling) providing only short passages of this cloud layer and the horizontal variability of ABM clouds as shown by Gayet et al. (2009). However, similar clouds have been investigated by McFarquhar et al. (2007); Shupe et al. (2006, 2008a) who observed ice crystals throughout the entire clouds by in situ and ground-based measurements. With the airborne remote-sensing techniques presented in this study, these findings could be confirmed by a third independent method.

Backscatter glories have been observed on top of the investigated clouds which generally indicates the presence of liquid water droplets at cloud top. This observation was validated by 3-D radiative transfer simulations focusing on the radiation within the backscatter region. Implementing ice crystals directly within the uppermost cloud layer (Case E) reproduced a weak but visible backscatter glory and explains the observations. Situating the thin ice layer above the original cloud (Case F) eliminated the backscatter glory.

These findings implicate that the presence of ice crystals within the cloud top layer alter the radiative properties of ABM clouds compared to values derived with the assumption of homogeneously mixed clouds. The cooling of the surface by such clouds due to enhanced reflection of solar radiation (e.g., Schweiger and Key, 1994; Dong and Mace, 2003; Ehrlich, 2009) might be stronger than calculated considering the enhanced side scattering of ice crystals. As the terrestrial infrared radiative forcing is determined by cloud temperature only and is almost unaffected by the vertical distribution of ice crystals, changes in the solar forcing propagate directly into the net (sum of solar and terrestrial) cloud forcing. The enhanced absorption by these ice crystals at solar wavelengths will also bias the ice indices utilized to identify the cloud thermodynamic phase (Acarreta et al., 2004; Ehrlich et al., 2008a). Compared to an upper cloud layer dominated by liquid water, a mixed-phase layer close to the top of ABM clouds biases the ice indices towards higher values.

The analysis of the spectral cloud-top reflectivity has shown that the spectral information within the wavelength range 1500–1800 nm is essential to retrieve information on ice crystal properties. In this regard the VWF of the SMART-Albedometer measurements was investigated using the methods described by Platnick (2000). The VWF $W(z)$ quantified the contribution of each cloud layer to the ice and liquid water absorption reflected in the measurements of R. The vertical profile of $W(z)$ showed that the measured signal is dominated by absorption processes within the uppermost cloud layers of less than 200 m thickness which is in agreement with the findings presented by Platnick (2000). However, $W(z)$ calculated for different wavelengths revealed spectral differences of the vertical weighting of the measurements. These differences result from the spectral pattern of ice and liquid water absorption. Consequently, by analyzing the spectral pattern of the measured R information on the vertical distribution of cloud particles can be retrieved.

Similar investigations have been conducted, e.g., by Chang and Li (2002, 2003) and Chen et al. (2008) who used four different wavelength bands of MODIS measurements (1250 nm, 1650 nm, 2150 nm and 3750 nm) to retrieve the vertical variation of cloud droplet effective diameter from remote sensing. The investigations presented in this study suggest that these methods are adaptive to high-resolution spectral measurements of a small wavelength region as obtained by the SMART-Albedometer. The only requirement is that the measurements resolve changes in the spectral absorption of ice and liquid water.

Acknowledgements. This research was funded by the German Research Foundation (DFG, WE 1900/8-1) and AWI. The Leibniz-Institute for Tropospheric Research, Leipzig, Germany is acknowledged for funding the integration of the SMART-Albedometer on the Polar 2 aircraft. We thank Ping Yang, Department of Atmospheric Sciences at Texas A&M University, for providing the library of optical properties of ice crystals used in our simulations. For the technical support during the ASTAR campaign we want to acknowledge the companies *enviscope* GmbH and OPTIMARE GmbH. Thomas Wagner and Steffen Beirle, both Max Planck Institute for Chemistry, Mainz, Germany, are thanked for the useful discussion that improved the quality of this paper.

Edited by: T. Garrett

References

Acarreta, J. R., Stammes, P., and Knap, W. H.: First retrieval of cloud phase from SCIAMACHY spectra around 1.6 μm, Atmos. Res., 72, 89–105, doi:10.1016/j.atmosres.2004.03.027, 2004.

Bierwirth, E., Wendisch, M., Ehrlich, A., Heese, B., Tesche, M., Althausen, D., Schladitz, A., Müller, D., Otto, S., Trautmann, T., Dinter, T., von Hoyningen-Huene, W., and Kahn, R.: Spectral surface albedo over Morocco and its impact on the radiative forcing of Saharan dust, Tellus, 61B, 252–269, 2009.

Boudala, F. S., Isaac, G. A., Cober, S. G., and Fu, Q.: Liquid fraction in stratiform mixed-phase clouds from in situ observations, Q. J. Roy. Meteor. Soc., 130, 2919–2931, doi:10.1256/qj.03.153, 2004.

Chang, F. L. and Li, Z. Q.: Estimating the vertical variation of cloud droplet effective radius using multispectral near-infrared satellite measurements, J. Geophys. Res., 107, 4257, doi:10.1029/2001JD000766, 2002.

Chang, F. L. and Li, Z. Q.: Retrieving vertical profiles of water-cloud droplet effective radius: Algorithm modification and preliminary application, J. Geophys. Res., 108, 4763, doi:10.1029/2003JD003906 , 2003.

Chen, R. Y., Chang, F. L., Li, Z. Q., Ferraro, R., and Weng, F. Z.: Impact of the vertical variation of cloud droplet size on the estimation of cloud liquid water path and rain detection, J. Atmos. Sci., 64, 3843–3853, 2007.

Chen, R. Y., Wood, R., Li, Z. Q., Ferraro, R., and Chang, F. L.: Studying the vertical variation of cloud droplet effective radius using ship and space-borne remote sensing data, J. Geophys. Res., 113, D00A02, doi:10.1029/2007JD009596, 2008.

CIE: Standard on colorimetric observers, Commission Internationale de lEclairage (CIE) cie s002 edition, 1986.

Cober, S. G., Isaac, G. A., Korolev, A. V., and Strapp, J. W.: Assessing cloud-phase conditions, J. Appl. Meteor., 40, 1967–1983, 2001.

Curry, J. A., Rossow, W. B., Randall, D., and Schramm, J. L.: Overview of Arctic cloud and radiation characteristics, J. Climate, 9, 1731–1764, 1996.

de Boer, G., Eloranta, E. W., and Shupe, M. D.: Arctic mixed-phase stratiform cloud properties from multiple years of surface-based measurements at two high-latitude locations, J. Atmos. Sci., 66, 2874–2887, 2009.

Dong, X. Q. and Mace, G. G.: Arctic stratus cloud properties and radiative forcing derived from ground-based data collected at Barrow, Alaska, J. Climate, 16, 445–461, 2003.

Ehrlich, A.: The impact of ice crystals on radiative forcing and remote sensing of arctic boundary-layer mixed-phase clouds, Ph.D. thesis, Johannes Gutenberg University Mainz, Germany, 2009.

Ehrlich, A., Bierwirth, E., Wendisch, M., Gayet, J.-F., Mioche, G., Lampert, A., and Heintzenberg, J.: Cloud phase identification of Arctic boundary-layer clouds from airborne spectral reflection measurements: Test of three approaches, Atmos. Chem. Phys., 8, 7493–7505, 2008a.

Ehrlich, A., Wendisch, M., Bierwirth, E., Herber, A., and Schwarzenböck, A.: Ice crystal shape effects on solar radiative properties of Arctic mixed-phase clouds – Dependence on microphysical properties, Atmos. Res., 88, 266–276, 2008b.

Fan, J., Ovtchinnikov, M., Comstock, J., McFarlane, S., and Khain, A.: Modeling Arctic mixed-phase clouds and associated ice formation, in: Proceedings of the ICCP Conference, Cancun, Mexico, 7–11 July, 2008.

Gayet, J. F., Mioche, G., Dornbrack, A., Ehrlich, A., Lampert, A., and Wendisch, M.: Microphysical and optical properties of Arctic mixed-phase clouds. The 9 April 2007 case study., Atmos. Chem. Phys., 9, 6581–6595, 2009, http://www.atmos-chem-phys.net/9/6581/2009/.

Gedzelman, S. D.: Simulating glories and cloudbows in color, Appl. Opt., 42, 429–435, 2003.

Harrington, J. Y., Reisin, T., Cotton, W. R., and Kreidenweis, S. M.: Cloud resolving simulations of Arctic stratus - Part II: Transition-season clouds, Atmos. Res., 51, 45–75, 1999.

Korolev, A. V., Isaac, G. A., Cober, S. G., Strapp, J. W., and Hallett, J.: Microphysical characterization of mixed-phase clouds, Quart. J. Roy. Meteor. Soc., 129, 39–65, 2003.

Lampert, A., Ehrlich, A., Drnbrack, A., Jourdan, O., Gayet, J.-F., Mioche, G., Shcherbakov, V., Ritter, C., and Wendisch, M.: Microphysical and radiative characterization of a subvisible midlevel Arctic ice cloud by airborne observations – a case study, Atmos. Chem. Phys., 9, 2647–2661, 2009, http://www.atmos-chem-phys.net/9/2647/2009/.

Lawson, R. P., Baker, B. A., Schmitt, C. G., and Jensen, T. L.: An overview of microphysical properties of Arctic clouds observed in May and July 1998 during FIRE ACE, J. Geophys. Res., 106, 14989–15014, 2001.

Mayer, B.: I3RC phase 1 results from the MYSTIC Monte Carlo model, in: Intercomparison of three-dimensional radiation codes: Abstracts of the first and second international workshops, University of Arizona Press, USA, 49–54, 1999.

Mayer, B.: I3RC phase 2 results from the MYSTIC Monte

Carlo model, in: Intercomparison of three-dimensional radiation codes: Abstracts of the first and second international workshops, University of Arizona Press, 107–108, 2000.

Mayer, B.: Radiative transfer in the cloudy atmosphere, The European Physical Journal Conferences, 1, 75–99, 2009.

Mayer, B. and Emde, C.: Comment on "Glory phenomenon informs of presence and phase state of liquid water in cold clouds" by Anatoly N. Nevzorov, Atmos. Res., 84, 410–419, 2007.

Mayer, B. and Kylling, A.: Technical note: The libRadtran software package for radiative transfer calculations - description and examples of use, Atmos. Chem. Phys., 5, 1855–1877, 2005, http://www.atmos-chem-phys.net/5/1855/2005/.

Mayer, B., Schröder, M., Preusker, R., and Schüller, L.: Remote sensing of water cloud droplet size distributions using the backscatter glory: A case study, Atmos. Chem. Phys., 4, 1255–1263, 2004, http://www.atmos-chem-phys.net/4/1255/2004/.

McFarquhar, G. M. and Cober, S. G.: Single-scattering properties of mixed-phase Arctic clouds at solar wavelengths: Impacts on radiative transfer, J. Climate, 17, 3799–3813, 2004.

McFarquhar, G. M. and Heymsfield, A. J.: The definition and significance of an effective radius for ice clouds, J. Atmos. Sci., 55, 2039–2052, 1998.

McFarquhar, G. M., Zhang, G., Poellot, M. R., Kok, G. L., Mccoy, R., Tooman, T., Fridlind, A., and Heymsfield, A. J.: Ice properties of single-layer stratocumulus during the Mixed-Phase Arctic Cloud Experiment: 1. Observations, J. Geophys. Res., 112, D24201, 2007.

Morrison, H., Curry, J., and Khvorostyanov, V.: A new double-moment microphysics parameterization for application in cloud and climate models. Part II: Single-column modeling of Arctic clouds, J. Atmos. Sci., 62, 1678–1693, 2005.

Morrison, H., Pinto, J. O., Curry, J. A., and McFarquhar, G. M.: Sensitivity of modeled Arctic mixed-phase stratocumulus to cloud condensation and ice nuclei over regionally varying surface conditions, J. Geophys. Res., 113, doi:10.1029/2007JD008729, D05203, 2008.

Pinto, J. O.: Autumnal mixed-phase cloudy boundary layers in the Arctic, J. Atmos. Sci., 55, 2016–2038, 1998.

Platnick, S.: Vertical photon transport in cloud remote sensing problems, J. Geophys. Res., 105, 22919–22935, 2000.

Prenni, A. J., Harrington, J. Y., Tjernstrom, M., DeMott, P. J., Avramov, A., Long, C. N., Kreidenweis, S. M., Olsson, P. Q., and Verlinde, J.: Can ice-nucleating aerosols affect Arctic seasonal climate?, B. Am. Meteor. Soc., 88, 541–550, 2007.

Schweiger, A. and Key, J.: Arctic ocean radiative fluxes and cloud forcing estimated from the ISCCP C2 cloud dataset, 1983-1990, J. Appl. Meteorol., 33, 948–963, 1994.

Shupe, M. D. and Intrieri, J. M.: Cloud radiative forcing of the Arctic surface: The influence of cloud properties, surface albedo, and solar zenith angle, J. Climate, 17, 616–628, 2004.

Shupe, M. D., Matrosov, S. Y., and Uttal, T.: Arctic mixed-phase cloud properties derived from surface-based sensors at SHEBA, J. Atmos. Sci., 63, 697–711, 2006.

Shupe, M. D., Daniel, J. S., de Boer, G., Eloranta, E. W., Kollias, P., Long, C. N., Luke, E. P., Turner, D. D., and Verlinde, J.: A focus on mixed-phase clouds: The status of ground-based observational methods, Bull. Amer. Meteor. Soc., 89, 1549–1562, 2008a.

Shupe, M. D., Kollias, P., Persson, P. O. G., and McFarquhar, G. M.: Vertical motions in Arctic mixed-phase stratiform clouds, J. Atmos. Sci., 65, 1304–1322, 2008b.

Stamnes, K., Tsay, S., Wiscombe, W., and Jayaweera, K.: A numerically stable algorithm for discrete-ordinate-method radiative transfer in multiple scattering and emitting layered media, Appl. Opt., 27, 2502–2509, 1988.

Turner, D. D., Ackerman, S. A., Baum, B. A., Revercomb, H. E., and Yang, P.: Cloud phase determination using ground-based AERI observations at SHEBA, J. Appl. Meteor., 42, 701–715, 2003.

Warren, S. G. and Brandt, R. E.: Optical constants of ice from the ultraviolet to the microwave: A revised compilation, J. Geophys. Res., 113, D14220, doi:10.1029/2007JD009744, 2008.

Wendisch, M., Müller, D., Schell, D., and Heintzenberg, J.: An airborne spectral albedometer with active horizontal stabilization, J. Atmos. Oceanic Technol., 18, 1856–1866, 2001.

Wieliczka, D. M., Weng, S. S., and Querry, M. R.: Wedge Shaped Cell For Highly Absorbent Liquids – Infrared Optical-Constants Of Water, Appl. Opt., 28, 1714–1719, 1989.

Yang, P. and Liou, K. N.: Finite-difference time domain method for light scattering by small ice crystals in three-dimensional space, J. Opt. Soc. Am. A., 13, 2072–2085, 1996.